

Simulations of a comet impact on the Moon and associated ice deposition in polar cold traps

Bénédicte D. Stewart^{a,*}, Elisabetta Pierazzo^b, David B. Goldstein^a, Philip L. Varghese^a, Laurence M. Trafton^c

^a Department of Aerospace Engineering, The University of Texas at Austin, 1 University Station C0600, Austin, TX 78712-0235, United States

^b Planetary Science Institute, 1700 E. Fort Lowell Rd., Suite 106, Tucson, AZ 85719, United States

^c Department of Astronomy, The University of Texas at Austin, 1 University Station C1400, Austin, TX 78712-0235, United States

ARTICLE INFO

Article history:

Received 9 November 2010

Revised 11 March 2011

Accepted 11 March 2011

Available online 21 March 2011

Keywords:

Atmospheres, Dynamics

Impact processes

Moon

ABSTRACT

Modeling results of the water vapor plume produced by a comet impact on the Moon and of the resulting water ice deposits in the lunar cold traps are presented. The water vapor plume is simulated near the point of impact by the SOVA hydrocode and in the far field by the Direct Simulation Monte Carlo (DSMC) method using as input the SOVA hydrocode solution at a fixed hemispherical interface. The SOVA hydrocode models the physics of the impact event such as the surface deformation and material phase changes during the impact. The further transport and retention processes, including gravity, photodestruction processes, and variable surface temperature with local polar cold traps, are modeled by the DSMC method for months after impact. In order to follow the water from the near field of the impact to the full planetary induced atmosphere, the 3D parallel DSMC code used a collision limiting scheme and an unsteady multi-domain approach. 3D results for the 45° oblique impact of a 2 km in diameter comet on the surface of the Moon at 30 km/s are presented. Most of the cometary water is lost due to escape just after impact and only ~3% of the cometary water is initially retained on the Moon. Early downrange focusing of the water vapor plume is observed but the later material that is moving more slowly takes on a more symmetric shape with time. Several locations for the point of impact were investigated and final retention rates of ~0.1% of the comet mass were observed. Based on the surface area of the cold traps used in the present simulations, ~1 mm of ice would have accumulated in the cold traps after such an impact. Estimates for the total mass of water accumulated in the polar cold traps over 1 byr are consistent with recent observations.

© 2011 Elsevier Inc. All rights reserved.

1. Introduction

Water has been deposited on the lunar surface throughout the Moon history from sources such as liberation from the lunar interior, solar wind bombardment, as well as cometary, meteorite and micrometeorite impacts. However, the present distribution of water on the lunar surface remains uncertain. The mean lunar daylight surface temperature is believed to be too high for large water ice deposits to accumulate at low latitudes. At high latitudes, however, due to the low inclination of the Moon's spin axis for the past 2 byr (Arnold, 1979), the bottom of some craters near the poles may never see the sunlight and have temperatures low enough (Vasavada et al., 1999) to capture and retain water molecules over geologic times (Watson et al., 1961). Large quantities of water ice within these permanently shaded regions, called cold traps, could be used to sustain long term human missions on the lunar surface.

Over the years, observation and modeling efforts have been looking for water on the Moon, and more specifically at the lunar poles.

Backscatter observations using the Earth-based 13-cm wavelength (Stacy et al., 1997), and 70-cm wavelength (Campbell et al., 2003; Campbell and Campbell, 2006) Aricebo radar as well as the 3.5-cm Goldstone radar (Margot et al., 1999) were unable to establish conclusively that water ice deposits exist near the lunar poles. A related bistatic radar experiment by the Clementine spacecraft also seemed to be inconclusive with small patchy ice deposits (Nozette et al., 1996) and surface roughness as possible explanations for the observations (Simpson and Tyler, 1999). From these radar experiments, the absence of a strong signature and the lack of correlation between the regions of enhanced backscatter and locations of the cold traps suggest the absence of thick ice deposits. However, water mixed with regolith at a concentration of 1–2% could still be present near the poles (Simpson and Tyler, 1999; Campbell et al., 2003).

Two years after Clementine, the neutron spectrometer experiment onboard Lunar Prospector observed enhanced deposits of hydrogen at the poles with locations consistent with permanently

* Corresponding author.

E-mail address: larignonb@gmail.com (B.D. Stewart).

shadowed areas (Feldman et al., 1998, 2000). The strength of the signature may be consistent with deposits of about 1.35×10^8 and 0.62×10^8 tons of water ice at the South and North Poles, respectively, at a mass fraction of water of $1.5 \pm 0.8\%$ within the regolith. Soon after, other groups questioned Feldman et al.'s findings and attributed the neutron spectrometer observations to either the presence of trapped protons (Starukhina and Shkuratov, 2000) or the deficit or excess of some minerals, such as CaO or SiO₂, in the regolith (Hodges, 2002) at the poles. More recently, Lawrence et al. (2006) argued that Hodges' hypothesis was inconsistent with the current knowledge of elemental concentrations at the lunar surface and that hydrogen deposits, possibly in water form, were the origin of the observation made by Lunar Prospector. A few years later, Eke et al. (2009) reconstructed an image of the distribution of hydrogen at the poles from the Lunar Prospector data. They showed that the hydrogen deposits observed at the lunar poles were not uniform but mostly localized inside the polar cold traps. Because large water ice deposits can only be stable over long period of times inside the lunar cold traps, Eke et al.'s findings (2009) would be consistent with water ice deposits.

Within the last year, three fly-by or orbiter missions have reported extended deposits of low concentrations of adsorbed water or OH over most of the lunar surface. The Visual and Infrared Mapping Spectrometer (VIMS) onboard Cassini (Clark, 2009), the HRI-IR Spectrometer onboard Deep Impact (Sunshine et al., 2009), and the Moon Mineralogy Mapper (M³) spectrometer onboard Chandrayaan-1 (Pieters et al., 2009) detected global features within the hydration wavelengths of 2.7–3.0 μm . All three observation data sets displayed stronger signatures toward the poles but adsorbed water or OH were observed at all latitudes. The spectrometer data showed much more extended water and OH coverage than the Lunar Prospector data. However, the results were not mutually exclusive because the neutron spectrometer detected large deposits up to 1 m deep and the visual and infrared spectrometers detected a thin layer down to at most a few millimeters thick at the lunar surface which would have been invisible to the neutron spectrometer onboard Lunar Prospector (Clark, 2009; Pieters et al., 2009). Due to the global coverage of the deposits and because of the rapid photodestruction of water in the atmosphere, solar wind bombardment of the lunar surface was argued to be the most probable source for the observed adsorbed water or OH (Sunshine et al., 2009; Pieters et al., 2009). Even more recently, the Lunar Crater Observation and Sensing Satellite (LCROSS) mission went a step further by impacting a Centaur rocket upper stage into the Cabeus crater, a possible water ice reservoir, in order to observe water and water by-products in the impact-induced plume (Colaprete et al., 2010; Schultz et al., 2010). Using data from near infrared and ultraviolet/visible spectrometers onboard the LCROSS Shepherding Spacecraft, Colaprete et al. observed the presence of water vapor, water ice and water photodissociation product OH in the ejecta plume. Colaprete et al. (2010) estimated that the concentration of water at the impact site was $\sim 5.6 \pm 2.9\%$ by mass, while Schultz et al. (2010) pointed out that the variety of volatiles released by the impact suggest that solar wind bombardment was not the only source for the water ice in the polar cold traps.

In parallel with the observations, modeling work has been investigating the relative contribution of the water sources and transport and destruction mechanisms involved during the water lifetime on the Moon. Using knowledge of the Moon gained from the Apollo missions, Arnold (1979) considered that the most probable sources for the lunar water were from solar wind reduction of Fe⁺⁺ in the regolith, from meteorites containing H₂O and from comet impact. In 1991, Morgan and Shemansky (1991) and Hodges (1991) looked at the limiting processes for the transport and accumulation of water in the polar cold traps. Hodges noted that photodestruction should be a limiting factor on the quantity of water

that reaches the cold traps. Morgan and Shemansky (1991) noted that the limiting loss process inside the cold traps was the Lyman α flux from the Local Interstellar Medium (LISM).

Recent works have used numerical methods to study the accumulation of water into the lunar cold traps (Butler, 1997; Crider and Vondrak, 2000, 2002) and the retention processes within the cold traps (Crider and Vondrak, 2003). Using a Monte Carlo approach, Butler (1997) modeled the transport of water molecules over the surface of the Moon to the polar cold traps. Butler (1997) assumed uniformly distributed water molecules that hopped around the Moon until they were destroyed due to photodestruction processes or were captured by a cold trap. Using reasonable values for the photodestruction mean time under lunar conditions and for the surface area of the cold traps, he found that 20–50% of molecules would be captured by the cold traps. Crider and Vondrak (2000) used a similar Monte Carlo method to investigate the amount of hydrogen that would have reached cold traps over millions of years from solar wind bombardment of the lunar surface. They found that an average of 4.2% of initially uniformly distributed water molecules would reach a cold trap. Because 1% of all the incident solar wind protons hitting the lunar surface produce water, only 0.04% of the incident protons would reach a cold trap as water (Crider and Vondrak, 2002). In 2003, Crider and Vondrak refined their study by adding loss mechanisms for deposits inside the lunar cold traps. They found a final retention rate of water of 5.6%. Over the trapping period of a billion years, water created by the solar wind bombardment of the lunar surface would be sufficient to account for the expected quantity of water present in the lunar cold traps (Crider and Vondrak, 2003) based on the Lunar Prospector data (Feldman et al., 2000).

Looking at comet impacts, Morgan and Shemansky (1991) estimated the average time between impacts to be about 13.3 myr with an average incoming comet mass of about 7×10^{16} g. Based on impact experiments, they estimated that 75% of that water would be lost because of dissociation and direct escape within the early plume. Assuming that 1 in 20 molecules reach the cold traps, 1.8×10^9 tons of water should reach the cold traps due to comet impacts which should cover 1 cm of estimated permanently shadowed regions. In 1998 (Berezhnoi and Klumov, 1998), Berezhnoi and Klumov considered a comet impact as the possible source for the hydrogen signature detected at the lunar poles by Lunar Prospector (Feldman et al., 1998). Assuming a uniform expansion model with a known chemical composition similar to that expected after an impact event, they found that a comet, 2 km in diameter, impacting the Moon would have deposited enough water inside the polar cold traps to account for the Lunar Prospector observations. More recently, Ong et al. (2010) used hydrocode simulations to estimate the amount of water deposited on the Moon over 1 byr due to comet impacts. They first estimated the retention rate of water after impact by accounting for the material with velocities smaller than the escape velocity of the Moon near the point of impact. Ong et al. found that nearly all of the water was retained for low impact velocities (for a 5 km/s impact) but nearly all of the water was lost at much higher velocities (for a 60 km/s impact). Because their numerical domain extended to only a few tens of kilometers above the surface they used data from Butler (1997) and Crider and Vondrak (2003) computations in order to estimate the transport and cold trap losses for the remaining water. Using estimates of the flux and distribution size of comets that would have impacted the Moon over a 1 byr period, they estimated that between 1.3×10^8 and 4.3×10^9 tons of water could have accumulated in the lunar cold traps over that period of time.

The Monte Carlo approaches used by Butler (1997) and Crider and Vondrak (2000, 2002) were valid for the slow accumulation of water in the cold traps. After a comet impact, however, the transport and deposition processes will be significantly different.

For relatively large comet impacts, the density of the initial gas is large enough so molecular collisions cannot be ignored, and the collisionless migration model to the cold traps used in the previous Monte Carlo approaches is no longer valid. Also, the amount of gas released may create a transient atmosphere that may partially shield the water molecules from photodestruction processes while in-flight (Arnold, 1979). Furthermore, the water molecules reaching the cold traps may be partially preserved through burial as the destruction rate of water ice by Lyman α radiation is smaller than the creation rate of new regolith (Morgan and Shemansky, 1991). To date, no modeling work has followed the cometary water from the time of impact until it is lost or deposited into the lunar cold traps. In the present work, SOVA hydrocode simulations of the impact event are directly interfaced with the DSMC method which then models the late stages of the event and the induced atmospheric flow. Below, we first describe the basic features of both the SOVA and DSMC codes. Next, the interface between the SOVA and DSMC codes is introduced and discussed. Afterwards, we present the three-dimensional results for a 45° oblique impact on the lunar surface. Results from a few seconds after impact to several months later are presented. Finally, the influence of the point of impact location on the deposition patterns of water in the polar cold trap is investigated.

2. Numerical method

The vapor plume produced during a comet impact on the Moon expands from a high density supersonic flow near the impact point to a free molecular circum-lunar flow weeks to months after the impact. The use of a hybrid SOVA–DSMC method enables us to resolve both the physics of the impact event as well as the physics of non-equilibrium transitional to rarefied flows minutes to months later. The SOVA hydrocode is used to solve the high deformation physics and phase changes during the first few seconds after impact. Using the data from the SOVA simulations, the DSMC code then simulates the expanding water vapor flow and follows the cometary water until it is lost or captured inside a cold trap.

2.1. The SOVA hydrocode

Shock codes, also generally known as hydrodynamic computer codes, or hydrocodes (Anderson, 1987), are used to simulate numerically highly dynamic events that include shocks. Hydrocodes solve the system of highly non-linear equations that describe the shock event, based on the conservation of mass, momentum and energy combined with material models, equation of state and strength, necessary to describe the material response. The equation of state is critical for describing the material responses in the early stages of the impact, when the main component of stress is pressure, the volumetric stress. It relates a material's instantaneous pressure, mass density and internal energy (and ideally the temperature and entropy as well). The equations of state define various thermodynamic properties of a material, such as compressibility, wave speed and thermal expansion, and should provide some description of phase changes. The final characteristics of an impact crater are highly dependent on the material strength model that links the strain of deformation to the deviatoric stress (e.g., see Pierazzo et al. (2008), for a review).

The hydrocode used for this study is SOVA (Shuvalov, 1999) an Eulerian code that can be run in different modes of geometry (planar, cylindrical, spherical) and dimensionality (1D, 2D, 3D). SOVA uses a tabular version of the ANEOS equation of state (Thompson and Lauson, 1972; Melosh, 2007) to model the behavior of the materials used in the impact. The simulations for this study concentrate on the early stage of the impact, focusing on the propaga-

tion of the shock wave, the internal energy and temperature, as well as melting and vaporization of material. The late stage of cratering, namely the cessation of excavation and crater collapse, is not of interest, thus a strength model was not required for these simulations (Pierazzo and Melosh, 2000a, 2000b; Artemieva and Shuvalov, 2008; Pierazzo et al., 2008). In addition to the macroscopic data obtained with the Eulerian solver, such as density, velocity, and temperature, the time evolution of the material can be followed by massless Lagrangian tracers initially distributed in both the target and the impactor.

For this work, SOVA was modified to output time-dependent data from a given set of (fixed) cells. These cells form the interface used to transfer data from the SOVA simulations to the DSMC computations. We chose cells on a hemispherical interface several cells thick centered at the impact point. For each cell SOVA records the concentration, density, partial pressure, temperature and bulk velocity of the materials present within the cell. The choice of the hemisphere interface was a compromise between two requirements. On one hand, the hemisphere had to be far enough from the impact point that gas densities in the selected cells are low enough to reduce the computational cost of the DSMC simulations to a reasonable level. On the other hand, SOVA describes material as a continuum and cannot simulate accurately very low densities, thus the need to have a very tenuous atmosphere ($\sim 5 \times 10^{-6}$ kg/m³) above the lunar surface as initial condition in SOVA. Based on Ong et al.'s findings (2010), this value is not expected to influence the shape of the expansion plume. Furthermore, given the high resolution required for early time simulations, the computational cost of SOVA increases rapidly with increasing domain size. As a result, in the following simulations, a mid-range interface was chosen in order to optimize the total computational time.

2.2. The DSMC method

For most common problems, gas flows can be modeled by the Navier–Stokes equations. However, when the mean free path of the gas becomes of the order of some representative length scale of the problem, the continuum assumption breaks down and the flow has to be represented by the Boltzmann equation. Unfortunately, the Boltzmann equation cannot generally be solved analytically due to the large number of unknowns and the difficulty of modeling the collision integral (especially for inelastic collisions). Therefore a molecular computational approach, such as the Direct Simulation Monte Carlo (DSMC) method (Bird, 1994), is generally chosen to solve non-continuum flows. The DSMC method models gas flows at the microscopic level using representative molecules. These simulated molecules are created and moved inside a meshed domain and typically each simulated molecule represents a large number of real molecules ($O(10^{20}–10^{30})$). The interactions between molecules are processed through modeled binary collisions of neighboring molecules. For a large number of representative molecules, the basic DSMC collision models have been shown to accurately represent the collision integral of the Boltzmann equation (Nanbu, 1986). The DSMC method is inherently unsteady and at predetermined intervals, the molecular data can be sampled to obtain the macroscopic quantities of interest such as density, temperature and velocity. The advantages of the DSMC method are that it can include physical mechanisms such as internal energy exchange and radiative cooling relatively easily, and is well suited for parallelization. During the intermediate stages of a comet impact event on an airless body such as the Moon, as the vapor plume of water expands away from the point of impact, the flow rapidly evolves from continuum to rarefied. Also, the small fraction of the water remaining on the Moon after impact will stay collisional near the dawn terminator up to weeks after impact. As the Moon rotates around its axis, the Sun rises over ice deposits on

the lunar nightside sustaining a relatively thicker atmosphere around the dawn terminator as it moves along the lunar surface (Goldstein et al., 2007). Therefore, the DSMC method is well suited to solve the intermediate flow regimes occurring between the early high density flow near the point of impact and the late free molecular flow established months later.

2.2.1. Overview of the present DSMC implementation

The present DSMC code is an extension of the axisymmetric code Zhang et al. (2003, 2004) used to simulate the sublimation atmosphere and volcanic plumes on Jupiter's moon Io. The current implementation retains some of the original code specific features such as a variable gravity field, multiple species (including solid grains and condensates), internal energy exchange, and radiation from the rotational and quantized vibrational lines (Zhang et al., 2003, 2004). The present DSMC code is fully 3D and, expanding on the previous axisymmetric implementation, a molecule location is given in spherical coordinates by its radial distance from the center of the planet, r , and its polar and azimuthal angles from the axis of symmetry, θ and ϕ , respectively (Fig. 1). A more complete description of the present implementation can be found in Stewart et al. (2009).

DSMC simulations are not subject to the standard stability constraints of other numerical approaches but both timestep and cell sizes have to be chosen carefully to obtain meaningful results. It is preferable for the timestep size to be smaller than the flow mean collision time and for the cell size to be of the order the mean free path in order to resolve a flowfield accurately. However, these conditions cannot be met near the interface with the SOVA hydrocode where the mean free path is of the order a few microns. Because we are mostly interested in the far field deposition of the water, an approximate approach to modeling the dense transitional regions in the DSMC domain was deemed acceptable. Hence, we choose to use an under-resolved DSMC solution with large cells and large timestep in the near field as a transition to a resolved far field DSMC solution. The overall effect of such an approximation is to misrepresent the transport coefficients (e.g., the effective viscosity is too large). Fortunately, the gradients of the flow are small, with length scales far greater than the cell size in the under-resolved regions of the flow and hence errors in the transport coefficients have a minimal effect on the flow. In addition, the inviscid SOVA code (aside from numerical viscosity) produces gradients only across its $O(10\text{ m})$ sized cells. Since the flow is rapidly expanding, these lateral and radial gradients are dissipating fast so the under-resolved DSMC solution can track them effectively.

The relaxation of timestep and cell size requirements means that a large number of collisions must be computed in every cell at each timestep. In general, in the local thermal equilibrium (L.T.E.) regions, some fraction of the total number of collisions brings the flow to equilibrium and the remainder only redistributes energy at the microscopic level leaving the macroscopic variables unchanged. For a gas in thermal equilibrium, the translational and rotational energy modes of a molecule reach equilibrium with the other molecules in a cell after usually only a few collisions, while the vibrational modes require anywhere from $\sim 10^2$ to 10^4 collisions to equilibrate. Therefore, a collision limiter can be used in the high density regions of the flow in L.T.E. to decrease the computational time without significant loss of accuracy relative to a resolved DSMC calculation (Titov and Levin, 2007; Macrossan and Geng, 2007; Stewart et al., 2009). In the present simulations, a two-level collision limiter is used where the rotational and translational modes are equilibrated first using regular collisions, then the vibrational modes are brought to equilibrium using “modified” collisions where vibrational energy exchange is forced. Each one of these collisions represents hundreds of regular collisions and enables faster computation of the equilibration of the vibrational energy modes of a molecule. Further away from the point of impact, where the collision rate of the flow decreases, the collision limiting scheme relaxes to the regular DSMC collision scheme when the number of collisions to compute decreases below the collision limit (Stewart et al., 2009). Finally, because of the spherical geometry, the cell size increases with altitude and towards the equator. For this reason, the code uses a free cell subroutine that only collides close-by molecules (Roveda et al., 2000).

Even with the use of the collision limiting scheme, the simulations of the expansion plume produced by a comet impact and of the induced transient atmosphere around the Moon remained computationally expensive. For this reason, a parallel version of the code was run on the Texas Advanced Computing Center (TACC) supercomputers Lonestar and Ranger using the Message Passing Interface (MPI) implementation. The DSMC method is well suited to parallelization (Dietrich and Boyd, 1996; LeBeau, 1999; Wu and Tseng, 2005) because the representative molecules only interact (through collisions) with other molecules in their cell. Therefore, a parallel implementation of the DSMC method only requires a decomposition of the physical domain between the processors. Then each processor creates, moves, and collides its own set of molecules. For computational efficiency reasons, the number of communications between the processors is limited and a non-uniform static domain decomposition is used in the azimuthal direction. For an oblique impact, most of the material moves downrange of the impact point with relatively less mass flux in the crossrange and uprange directions. Using a low resolution run to estimate the workload associated with each azimuthal degree, a non-uniform domain decomposition was implemented where processors in the downrange direction only simulate 1° of azimuth while crossrange and uprange processors simulate up to 30° . Overall, the present implementation was shown to be relatively computationally efficient (Stewart et al., 2009).

2.2.2. DSMC domain

The cells closest to the point of impact need to be small enough to capture the physics of the expansion plume, at most a few hundreds of meters in each direction. However, it is currently impossible to run a full planet simulation with such small cells. For that reason, a multi-domain restart capability has been implemented in the code so that molecules created close to the point of impact can be transferred to a larger domain as they exit the inner domain. The first DSMC simulation is run inside a relatively small domain near the point of impact. As molecules exit this inner domain they are saved to a file to be read in a later simulation of the outer

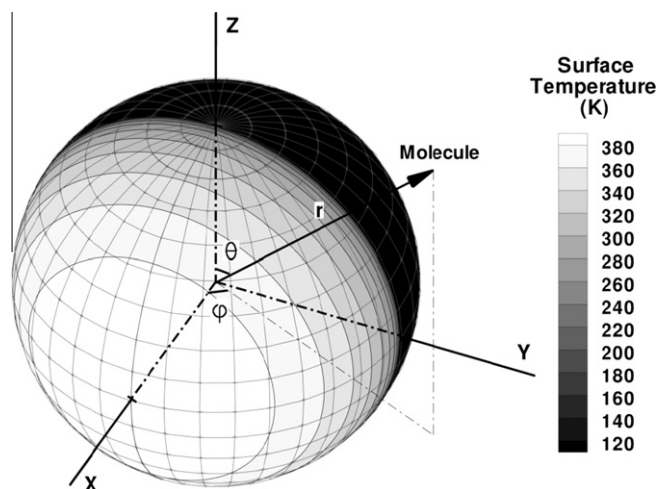


Fig. 1. Spherical coordinate system used for the DSMC simulations with the surface temperature distribution on the Moon.

domain. From each domain to the next, both timestep and cell sizes are increased but the unsteady fluxes at the boundaries of the inner domain match from one simulation to the next. This process is repeated until the entire Moon is simulated. This unsteady sequential multi-domain approach is valid for the early time DSMC simulations as the expansion flow produced by the comet impact is still supersonic. This method was validated by successfully matching macroscopic contours across boundaries between the inner and outer domains.

The impact point in all simulations is located at the axis of symmetry of the DSMC spherical grid (i.e. where r is the radius of the Moon and $\theta = 0$) to take advantage of the fine gridding in that region. This means that the point of impact and its antipode (if within the DSMC domain) are singularities. Using the plane of symmetry of the problem, the domain for the early time simulations of the vapor expansion plume covers only 180° in the azimuthal direction. For the innermost domains, the top and right boundaries are a few tens to a few hundreds of kilometers away from the point of impact and are assumed to be vacuum (Fig. 2). The molecules crossing the top and right walls are saved for the next run of the multi-domain approach. For the full Moon simulations, the top boundary is located far enough above the lunar surface, several thousands of kilometers, such that only molecules with a speed greater than the escape velocity reach that boundary. For all the simulations, the bottom boundary represents the lunar surface.

2.2.3. SOVA–DSMC interface

The DSMC molecules are created at the hemispherical interface with the SOVA hydrocode based on the SOVA data. SOVA's hemispherical interface is formed by a series of Cartesian cells that do not precisely overlap with the spherical DSMC cells. The Cartesian SOVA interface cells are used as reservoir cells for the DSMC molecules (Roveda et al., 2000; Lilley and Macrossan, 2003; Garcia and Wagner, 2006). First, an equilibrium distribution of molecules is created inside each reservoir cell based on the SOVA density, temperature and velocity within the cell. Then, newly created molecules are randomly distributed inside the SOVA cell and are allowed to drift into the spherical DSMC grid. The thermal velocity components are drawn from a Maxwellian distribution. The molecules are moved by a full timestep and only the molecules exiting the reservoir cells are kept. When using reservoir cells for an inflow boundary condition, the DSMC timestep must be small enough that not all of the molecules exit the reservoir cells. Since the time interval between outputs in the SOVA hydrocode is variable and may be relatively large, the DSMC timestep is independent and

generally smaller than the SOVA timestep. The properties at the interface are unsteady and the DSMC molecules are created at each timestep based on the SOVA data until the DSMC time catches up to the SOVA time.

2.2.4. Modeled physics

Currently, in the DSMC domain, target material (rock) is ignored and only one species, water, is being considered. This is an acceptable assumption as both materials are generally present in different regions of the expansion plume. Radiation, condensation into droplets and chemistry are not modeled and all the water that crosses the SOVA/DSMC interface is assumed to be in the vapor phase. In reality, as the hot vapor plume expands and begins to cool, the gases within the plume may start to condense. However, it is believed that for planetary scale impacts, up to 50% of water vapor may remain monomeric and never condense (Melosh, 1989). Recently, Zhong et al. (2005) and Li et al. (2009) have investigated the influence of condensation on the overall flowfield in an expansion using a modified DSMC method. But because of complexity of the condensation processes both in simple expansion plumes and in impact induced vapor plumes, no definitive answer exists. Therefore, while the influence of cluster formation may or may not be of importance within an impact expansion vapor plume, it is currently beyond the scope of this work to explore that influence.

Once the water molecules have drifted inside the DSMC domain, they are moved under a variable gravity field, following a ballistic trajectory between collisions, using a predictor–corrector method. Note that Coriolis effects were ignored in the present simulations because the rotation rate of the Moon is slow. When a molecule hits the surface of the Moon outside of the cold traps, the surface interaction is computed using the Langmuir (1916) and Frenkel (1924) model for the residence time of water on a water ice matrix:

$$t_{\text{reside}} = \nu_0^{-1} \times e^{\Delta H/kT} \quad (1)$$

where $\Delta H = 6.65 \times 10^{-20}$ J is the binding energy, k is the Boltzmann constant, $\nu_0 = 2.0 \times 10^{12} \text{ s}^{-1}$ is the lattice vibrational frequency of water within a water ice matrix and T is the surface temperature (Sandford and Allamandola, 1988).

The Moon's surface temperature at a given location depends on that location's relative position to the subsolar point as follows (Butler, 1997):

$$T = (T_{\text{MAX}} - T_{\text{MIN}}) \times [\max(0, \cos \beta)]^{1/4} + T_{\text{MIN}} \quad (2)$$

where $T_{\text{MAX}} = 400$ K, $T_{\text{MIN}} = 120$ K and β is the subsolar zenith angle.

Because of the relatively long timescales involved in the present problem, the surface temperature at any point on the Moon's surface varies with time in order to account for the rotation of the Moon (similar to the temperature dependence in Walker et al., 2010). In the present simulations, it is assumed that the Moon rotates around its polar axis (in reality the tilt of the Moon rotation axis is $\sim 1.5^\circ$) with a rotation rate of $2.463 \times 10^{-6} \text{ s}^{-1}$ which is equivalent to a synodic period of 29 days 12 h 37 min.

Cold traps are modeled as cold anomalies within the surface map where arriving molecules remain stuck for the remainder of the calculation. The latitude and longitude locations of the cold traps at the South Pole are based on the data presented in Table 1 in Elphic et al.'s (2007) paper. Noda et al.'s (2008) estimates for the actual shaded surface area were used to scale the cold traps to cover the estimated permanently shadowed surface areas. In the present model, the cold traps are disks, centered on the crater centers considered by Elphic et al. (2007), with a modified radius set to represent the actual surface area of the permanently shadowed areas (Table 1; also see Fig. 11). This approach is not an

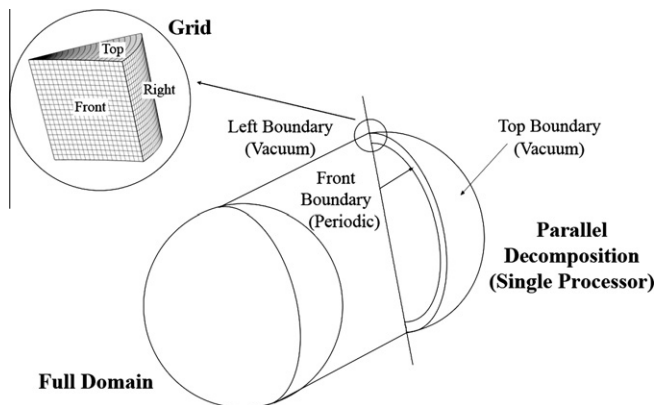


Fig. 2. Physical domain used in the DSMC simulations. Only three of the six boundaries of a single processor domain are shown (top, left and front boundaries) as the remaining three (bottom, right and back boundaries) are the respective opposite walls.

Table 1
Cold traps location and surface area (Elphic et al., 2007; Noda et al., 2008).

Crater name	Θ (°)	Φ (°)	Radius (km)	Surface area (km ²)
Unnamed (SP)	177.5	356	20.34	1300
Shoemaker	178.1	45	19.34	1175
Cabeus	174.5	322	16.93	900
Faustini	177.3	77	14.93	700
De Gerlache	178.5	273	9.77	300
Shackleton	179.7	110	7.98	200
Unnamed (NP)	1.7	312	20.0	1257

accurate representation of the shape of the permanently shaded regions within the craters, but it is adequate considering that the surface resolution for the full planet DSMC simulations is $1^\circ \times 1^\circ$ cells. At the North Pole, only one large trapping region around the 315° longitude is being considered with a radius consistent with Noda et al.'s (2008) observed shadowed area at the North Pole. Using these assumptions, the total surface area of the shadowed regions is 1257 km² at the North Pole and 4575 km² at the South Pole. These values are within 2.5% of the estimates of Noda et al. (2008).

The loss mechanisms modeled in the DSMC simulations are direct escape and photodestruction processes. Molecules in the sunlit part of the atmosphere may photodissociate or photoionize based on Huebner's (1992) probabilities, P , at 1 A.U. where Δt is the timestep size (Eq. (3)).

$$\begin{aligned} P_{\text{ionize}} &= e^{-\Delta t / 2.45 \times 10^6} \\ P_{\text{dissociate}} &= e^{-\Delta t / 8.3 \times 10^4} \end{aligned} \quad (3)$$

Note that recombination and neutralization are ignored so ions and dissociation products are deleted from the calculation.

3. Results and discussion

3.1. Simulations parameters

The present computations simulate the impact of a 2 km diameter water ice comet on the Moon at a velocity of 30 km/s and at a 45° angle from the lunar surface. The 3D SOVA simulations are carried out in a local Cartesian grid with the origin at the point of impact, and assume bilateral symmetry, which makes it possible to limit the model domain to the half space corresponding to $Y > 0$ (with $Y < 0$ being a mirror half space) starting from the impact plane (or symmetry plane), identified by the direction of impact and the perpendicular to the surface at the impact point. The SOVA computational domain extends 7 km below the surface to 38 km above, from 21 km in the uprange direction to 37 km in the downrange direction and from the plane of impact to 31 km in the cross-range direction. Non-uniform gridding is used in all three directions with the finest grid, using 50 m wide cells in all three directions, being localized to a central region around the impact point, corresponding to a resolution of 20 cells per projectile radius. For SOVA this resolution represents a good compromise between the need for high resolution to resolve the shock wave and the need to reduce the computational cost of SOVA by limiting the number of computational cells (Pierazzo et al., 2008). The cell size is incrementally increased in all three directions until the cell size reaches a maximum of 200 m in each direction. The comet itself is modeled as a water ice sphere (Turtle and Pierazzo, 2001) while the surface of the Moon has the material properties of granite (Pierazzo et al., 1997). For the purpose of this work, which focuses on the evolution of water above the lunar surface, granite is a reasonable approximation for a silicate body. In order to properly initialize the SOVA hydrocode simulations, a background atmosphere is initially present above the target surface. While

the actual gas density just above the surface of the Moon is of the order 10^{-14} kg/m³ (Stern, 1999), the background atmosphere density was chosen to be 5×10^{-6} kg/m³. Based on Ong et al.'s findings (2010), this value is not expected to influence the shape of the expansion plume since the plume densities are mostly much greater than this close to the impact point.

The SOVA–DSMC hemispherical interface is chosen to be 20 km away from the point of impact. The peak water vapor density at that distance is smaller than 0.8 kg/m³, small enough for the dilute gas assumption inherent to the DSMC method to apply (the validity of the simulation with DSMC was established by comparing the output of SOVA at 30 km from impact with the results of DSMC run using the SOVA input at the 20 km interface (Stewart et al., 2009)). The SOVA simulations were run until most of the cometary water had crossed the hemispherical interface, about 21 s after the beginning of the impact. The water present within the cells also containing some rock is ignored; at most 3% of all the water that crosses the interface is neglected as a consequence of this approximation. Most of that water would probably condense on adjacent dust grains and be removed from the water vapor expansion plume.

The ratio of real to simulated molecules (FNUM) in DSMC is 5×10^{29} and a series of five DSMC domains is used. Similar to the SOVA simulation, bilateral symmetry is used in the first four DSMC domains so only one half of the expansion plume is simulated. In the fifth domain, molecules are mirrored across the plane of symmetry in order to model the entire plume. The innermost domain is a $32 \text{ km} \times 32 \text{ km} \times 180^\circ$ pie sector with a cell size of 100 m and a timestep of 0.5 ms (Fig. 2). In this domain, the surface temperature near the impact point is low enough that molecules reside on the surface for a period comparable to the timescale of the near field calculation (~ 20 s). The radiative equilibrium boundary condition (Eq. (1)) is meant to handle only a thin precipitating layer; over time, a large amount of ejecta hitting the surface would warm up the lunar surface and water molecules would not remain on the surface for long. However, a negligible amount of water actually hits the surface near the impact point during the first few tens of seconds after impact, most of the ejecta consisting of rock excavated during crater formation (Fig. 3). The first intermediate domain is a $100 \text{ km} \times 100 \text{ km} \times 180^\circ$ pie sector with a cell size of 250 m and a timestep of 5 ms. The second intermediate domain is a $400 \text{ km} \times 400 \text{ km} \times 180^\circ$ piece of pie with a cell size of 1 km and a timestep size of 10 ms. The third intermediate domain is a $1000 \text{ km} \times 1000 \text{ km} \times 180^\circ$ pie sector with a 2.5 km cell size and a 50 ms timestep. For all four domains, a comparison between cell size and density based gradient length showed that while relatively large compared to the mean free path, the cell sizes were sufficient to capture the gradients of the flow. For the outermost domain, the top wall is located 50,000 km above the lunar surface so all molecules with a velocity slower than the escape velocity can be tracked.

The early time DSMC computations used 48 processors with a non-uniform domain decomposition while the outermost domain simulated the entire Moon using 36 processors with a uniform domain decomposition. A total of 100 million cells were used over the five domains and more than 150 million molecules were used to model the entire water vapor plume. The parallel computations of the expansion plume took ~ 1 month on 48 processors and the full planet simulations took ~ 3 days on 36 processors.

3.2. The water vapor expansion plume

The SOVA density distribution in the plane of symmetry of the impact is presented in Fig. 3, 1, 10 and 20 s after impact. Rock and water are represented in green and gray, respectively and darker shading represents denser material. The innermost black line represents the interface at which the SOVA data are provided for

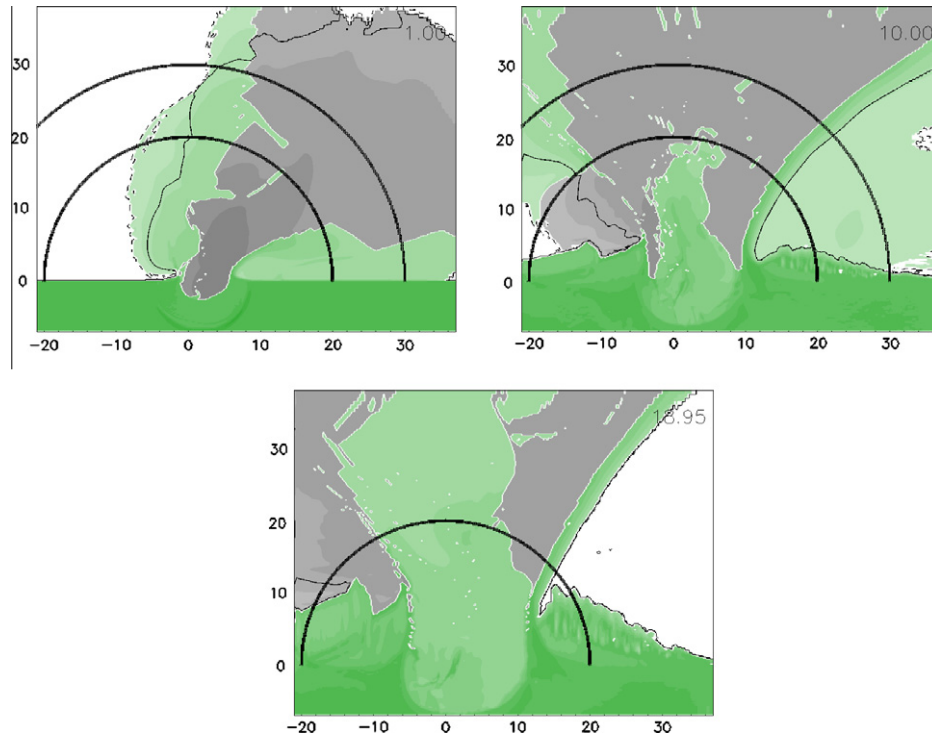


Fig. 3. Density shading in the plane of symmetry of the impact from a SOVA simulation 1, 10, and 20 s after a 45° impact of a comet 2 km in diameter at 30 km/s on the surface of the Moon.

the DSMC simulations. The outermost black line in the early time figures represents a test interface where SOVA data were compared to DSMC calculations. Two-dimensional (2D) projections of the DSMC water density and radial velocity contours at the 20 km transfer interface are shown on the left hand side and right hand side of Fig. 4, respectively, at the same time as the SOVA density distribution of Fig. 3. The point of view is from directly above the point of impact; so material farther away from the origin is also closer to the lunar surface. The red circle marks the intersection of the interface with the surface of the Moon. The DSMC solution for the half domain has been mirrored across the $\beta = 0^\circ$ plane to show the entire plume.

The water vapor plume undergoes several major shape changes during the early expansion phase. Initially, the plume is strongly directional, concentrating in the downrange direction (Fig. 4a and b). Beyond about ten seconds, however, the plume becomes more symmetric above the opening crater, which develops mostly downrange of the impact point (roughly centered about 4 km downrange of the impact point) and the plume begins to take the shape of an inverted cone (Fig. 4c). A secondary low density plume also appears uprange of the main high density plume. At the same time, a target-rich plume (green in the center of the SOVA density distribution figures) reaches the hemispherical interface. This expanding rocky plume is preceded by some relatively high density, high velocity water vapor that is moved out of the way as the rocky material rises directly above the opening crater (Fig. 4c and d). Twenty seconds after impact (Fig. 4e and f), the presence of the central rocky plume at the hemispherical interface causes the main water vapor plume to be largely confined to an outer ring. At the same time, the low density plume spreads uprange and eventually fills the entire uprange hemisphere.

3.3. Mass distribution inside the water vapor expansion plume

The DSMC simulations provide the exact number of simulated molecules entering the DSMC domain at each timestep at the

20 km hemispherical interface. From these data, the total mass and instantaneous mass flux of water through the interface can be studied as a function of time and azimuthal angle. The total fraction of comet mass through the interface and the fraction of water that crosses the interface through five angular sectors centered at azimuthal angles $\beta = 0, 45, 90, 135$, and 180° are shown in Fig. 5a as function of time. The instantaneous mass flux for the five different angular sectors and the total instantaneous flux of water at the interface are shown in Fig. 5b. Azimuthal angles $\beta = 0, 45, 90, 135$, and 180° represent the downrange, intermediate downrange, cross-range, intermediate uprange, and uprange directions, respectively.

The total mass of the comet is 4.65×10^{12} kg, and 21 s after the beginning of the expansion the total mass that has crossed the interface has asymptoted to $\sim 4.46 \times 10^{12}$ kg of water or $\sim 96\%$ of the total comet mass. Taking into account the $\sim 3\%$ of comet mass that was in mixed rock–water cells in the SOVA simulation and that was ignored in the DSMC simulation, the total amount of water remaining within the hemispherical interface 21 s after impact is $<1\%$ of the initial comet mass.

Fig. 5a provides important information about the rate of expansion of the vapor plume. For instance, it takes less than 2 s for half of the comet mass to cross the interface, with 90% of the comet mass crossing the interface in less than 10 s. This indicates that most of the cometary material is moving faster than the lunar escape velocity and will be blown off the Moon. The fastest material crosses the interface in under 0.4 s and therefore travels at nearly 50 km/s, assuming the water started to move outward at the point of impact. The maximum mass flux at the interface is achieved around 0.5 s after impact and lasts about 1 s (insert in Fig. 5b). During this time interval, the mass flux of water to cross the interface is $\sim 2 \times 10^{12}$ kg/s. A secondary peak can be observed about 9 s after impact. This secondary peak is believed to be due to the relatively high density water vapor moving directly above the point of impact (Fig. 4c). At the end of the SOVA simulation, the mass flux of water at the interface has dropped to $\sim 5 \times 10^9$ kg/s and the water vapor moves at velocities of only around 1 km/s (Fig. 4f).

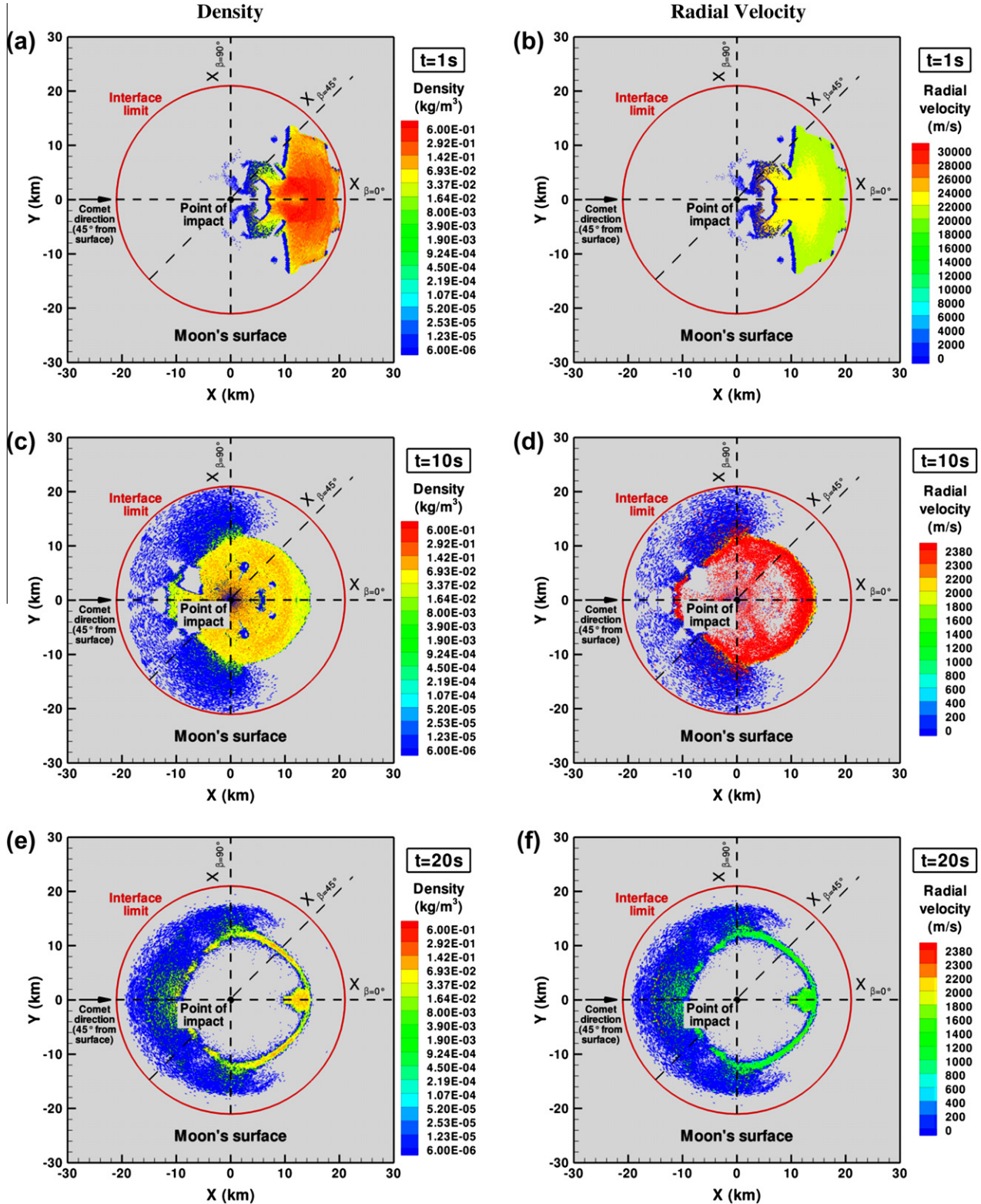


Fig. 4. DSMC density (left) and radial velocity (right) contours at the hemispherical interface 1, 10, and 20 s after impact. The red circle marks the intersection of the interface with the lunar surface. Note that the color legend for (b) is different than that for (d and e). Cells with velocities greater than the Moon's escape velocity at the lunar surface have been blanked out in (d and e).

Fig. 5 also provides additional information concerning the spatial mass loading of the water vapor plume. Initially, the water vapor plume travels preferentially in the downrange direction ($\beta = 0$ and 45°), crossing the interface 0.4 s after the beginning of the impact. In the crossrange direction ($\beta = 90^\circ$), the plume reaches the

interface after about 0.9 s and it takes an additional 0.7 s for the water to cross the interface uprange of the point of impact ($\beta = 135$ and 180°). About 50.2% of the comet mass moves directly downrange of the interface ($\beta = 0^\circ$) and 84.2% moves in the general downrange direction ($\beta = 0$ and 45°). The footprint of the plume is

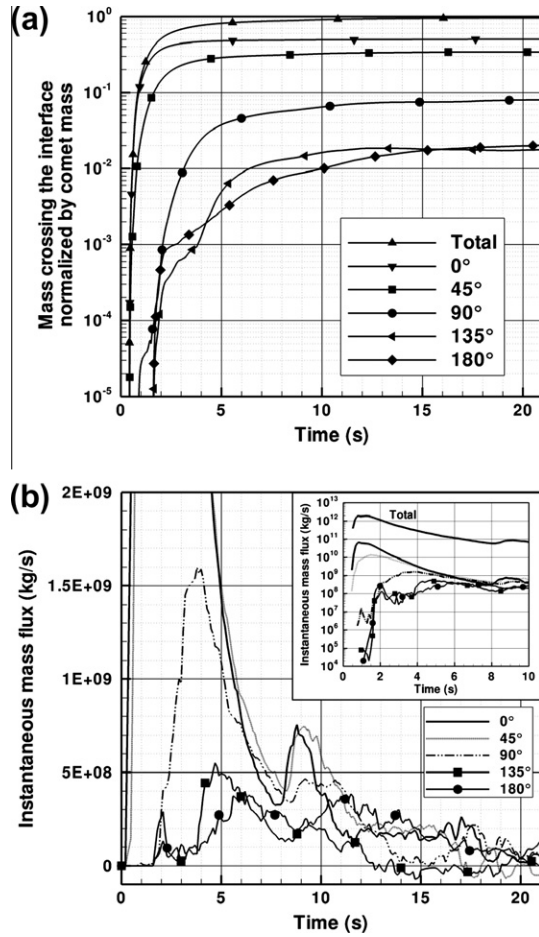


Fig. 5. Total and instantaneous mass of water that crosses the SOVA/DSMC hemispherical interface (20 km from the impact point) as a function of time. The comet mass was 4.65×10^{12} kg.

larger in the crossrange direction (Fig. 4c and e) but because the majority of the plume there is made out of low density material, the total mass of water crossing the interface in that plane is relatively small. Only 8% of the comet mass moves in the crossrange direction ($\beta = 90^\circ$) and even less water moves uprange with only 1.8% and 2% of the cometary water crossing the interface in the directions centered on $\beta = 135^\circ$ and $\beta = 180^\circ$, respectively.

The data shown in Fig. 5b are noticeably noisy; so, only the largest features are discussed in more detail below. In the downrange direction ($\beta = 0^\circ$), the peak instantaneous mass flux, at $\sim 7 \times 10^{10}$ kg/s, is observed between 0.6 and 1.3 s after impact. For all the other angular sectors, the peak instantaneous mass flux is observed later, from 1.5 to 4.5 s after impact, with peak values between $\sim 1.5 \times 10^{10}$ kg/s in the $\beta = 45^\circ$ direction and $4\text{--}5.5 \times 10^8$ kg/s in the other three directions. Secondary peaks are observed in all five regions between 8.5 and 11.5 s after impact. At later times, in the intermediate downrange ($\beta = 45^\circ$) and intermediate uprange ($\beta = 135^\circ$) directions, the mass flux begins to oscillate around zero. A negative instantaneous mass flux means that in that region more water is falling back through the interface towards the lunar surface than is rising above the interface. This represents a weak feedback from the DSMC domain to the SOVA domain. In the present hybrid coupling of SOVA and DSMC, the SOVA simulation is run first and the output is used as input to the DSMC simulations, assuming no feedback from the DSMC domain towards the SOVA domain. The total mass falling back through the interface is $\sim 0.3\%$ and $\sim 6.7\%$ of the total mass crossing the interface in the intermediate downrange ($\beta = 45^\circ$) and in the intermediate uprange ($\beta = 135^\circ$) regions, respectively. This amounts

about 0.1% of the total mass of water crossing the interface for the entire domain, hardly enough to have any effect on the plume expansion in SOVA. Therefore, the present sequential unidirectional calculations provide good estimates as to the total mass of water retained on the Moon after a comet impact.

3.4. Macroscopic properties within the water vapor expansion plume

Density, total temperature, radial velocity, and gradient based Knudsen number contours are presented in Figs. 6 and 7. The gradient based Knudsen number, Kn , is given by the ratio of the mean free path, λ (Eq. (4)), to the gradient length scale where the gradient length scale is approximated as the maximum between the value for the density gradient length in the horizontal (X_β) and vertical directions (Z_β):

$$\lambda = \frac{1}{\sqrt{2\pi}d^2n} \quad (4)$$

$$Kn_\lambda = \frac{\lambda}{\rho} \max \left(\left| \frac{d\rho}{dX_\beta} \right|, \left| \frac{d\rho}{dZ_\beta} \right| \right) \quad (5)$$

The data have been interpolated using an “inverse distance weighting” scheme with a sphere of influence 2 km in radius. In Fig. 6, the density contour plots are shown in the plane of symmetry of the impact ($\beta = 0^\circ, 180^\circ$), in the 45° intermediate plane ($\beta = 45^\circ, 135^\circ$) and in the plane perpendicular to the plane of symmetry of the impact ($\beta = 90^\circ$). With each contour plot, a small inset sub-figure shows the plane being considered. Total temperature, radial velocity with respect to the point of impact, and Knudsen number contours are presented in Fig. 7 in the plane of symmetry of the impact ($\beta = 0^\circ$) with a small inset sub-figure zooming closer to the point of impact.

Twenty-one seconds after impact, the largest plume is observed in the symmetry plane where some of the fastest moving material, which crossed the interface early on, has reached an altitude of ~ 900 km (Fig. 6). The plume also extends up to ~ 800 km downrange and ~ 100 km uprange of the point of impact, respectively. The density is largest just above the interface in the region of the plume directly above the rock dominated part of the plume, ~ 60 km above the lunar surface. A large region devoid of water is observed within the vapor plume ~ 350 km above the lunar surface and ~ 200 km downrange of the point of impact. This and other apparently “empty” regions are linked to SOVA cells containing target material mixed with the water vapor at earlier times. These “empty” cells have convected far downstream of the interface, but because of the very large velocities and relatively low thermal diffusion, the empty space has not yet been filled up with water. In the 45° intermediate plane, the plume up to ~ 300 km from the point of impact is very similar to that observed in the symmetry plane. Above ~ 300 km, the plume is very sparse and is mostly concentrated in two small sections, possibly due to initial jetting. Overall, the fastest water vapor has reached an altitude of ~ 800 km and the plume extends as far as ~ 600 km downrange and ~ 80 km uprange from the point of impact, respectively. In the intermediate plane, the density is again largest above the rock-dominated central region. In the plane perpendicular to the impact plane, the plume lateral extent is only one-fifth to one-sixth of the extent in the symmetry plane. The fastest material has reached an altitude of ~ 600 km and most of the water vapor is within ~ 200 km of the point of impact in the crossrange direction. Overall, the water vapor mostly moves straight up from the impact region and most of the water is located within ~ 300 km of the point of impact in that plane.

With asymmetry across the impact point, one of the most noticeable differences between an oblique impact plume and a

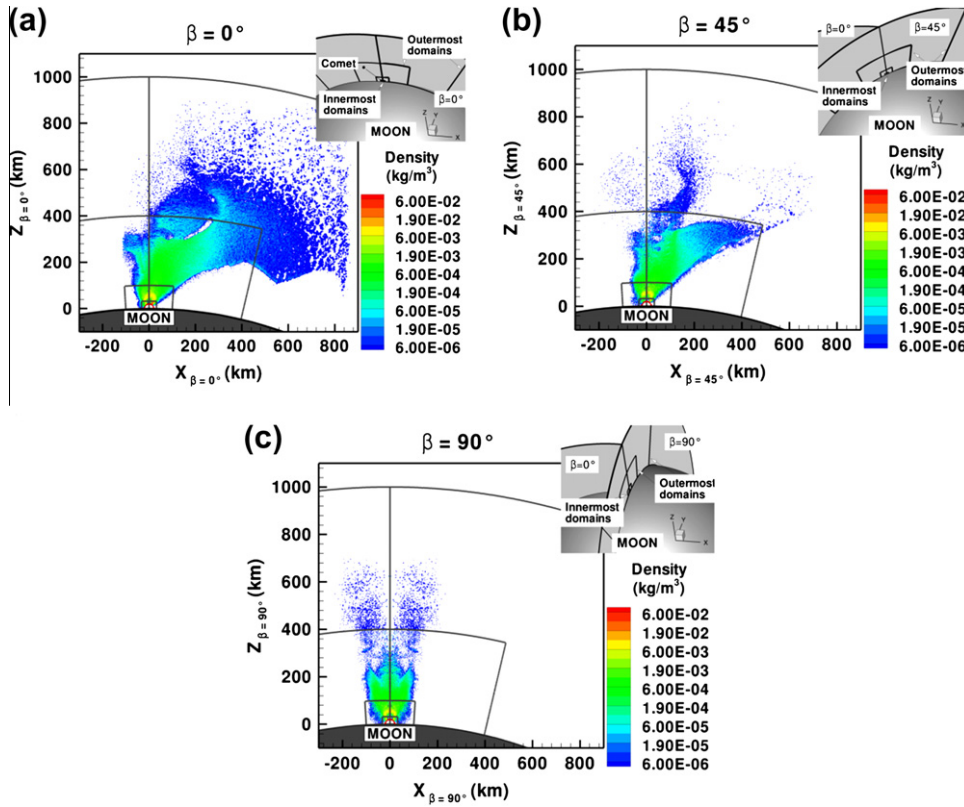


Fig. 6. Density contours 21 s after impact in: (a) the symmetry plane, (b) 45° off the symmetry plane and (c) perpendicular to the plane of symmetry (see inserts).

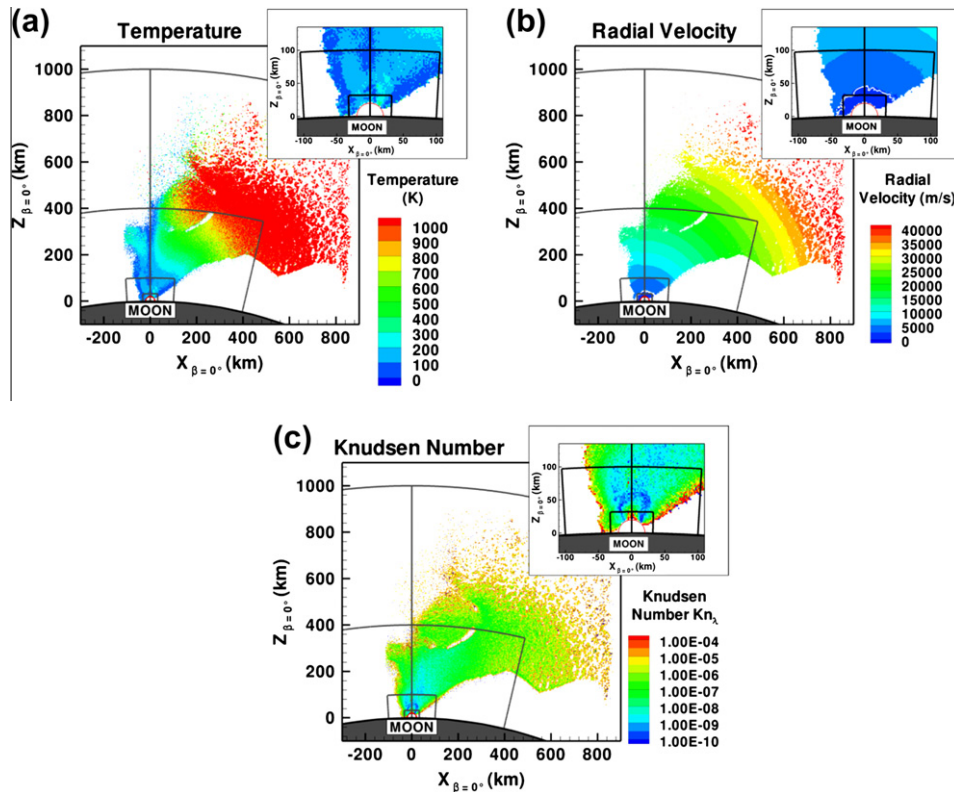


Fig. 7. (a) Total temperature, (b) radial velocity, and (c) Knudsen number contours 21 s after impact in the symmetry plane. Inserts show a zoomed in image of the same quantities.

simple spherical impulsive expansion flow is the temperature dependence on radial distance. In the present plume (Fig. 7a), the water vapor is hottest downstream (>1000 K). The cooling of the flow associated with the expansion of the gas is not sufficient to overcome the fact that outermost regions of the vapor plume were hotter than the innermost regions near the point of impact. Locally, a relatively warmer region is observed 60 km above the point of impact consistent with the relatively denser material observed above the rock-dominated region of the plume. Because the water vapor is still very dense within the entire plume, the flow is highly collisional and all the temperature components are still in equilibrium 21 s after impact.

In the radial velocity contours (Fig. 7b), the white line seen near the boundary of the innermost domain represents the locations at which the flow speed is equal to the escape velocity at the surface of the Moon (~ 2.38 km/s). All material above that line moves a speed higher than escape. Only a small region of the plume is below that white line so most of the water escapes the Moon gravity well. Overall, the radial velocity contours appear to be near concentric with the outermost, fastest material moving at more than 40 km/s (red region in Fig. 7b). With the present temperature distribution most of the plume is hypersonic 21 s after impact with the smallest Mach numbers being observed near the interface with the SOVA hydrocode where the water vapor is the slowest.

Overall, the Knudsen number (Fig. 7c) increases with radial distance but remains lower than 10^{-5} as far as 800 km from the point of impact, which places the flow entirely in the continuum regime. In the continuum regions of the flow, the total number of collisions to be computed in the DSMC domain would be prohibitive, but the use of the collision limiting scheme presented in Section 2.2.1 enables a relatively modest number of computations. The flow is collision limited within most of the plume 21 s after impact, but as the water vapor expands, the collision rate of the flow continues to decrease and the present collision limiting scheme eventually reverts to the standard DSMC collision routine (Stewart et al., 2009).

3.5. Initial retention rate

The “initial retention rate” of the expanding plume has been estimated by looking at the amount of water with speed smaller than the local escape velocity at the edge of the third intermediate domain. This approach accounts for possible deceleration of water vapor due to collisions. The mass of water in the vapor plume initially retained on the Moon after impact is about 2.1% of the comet mass. By accounting for the amount of water that remained within the interface 21 s after impact, the total retention rate for the water after the impact is about 3.1%. This estimate for the mass retained is consistent with recent results Ong et al. (2010) obtained by comparing the plume velocity at the edge of their domain to the escape velocity. Using results from their hydrocode simulations, they estimated that the fraction of water retained on the Moon after a vertical comet impact at 30 km/s was equal to $\sim 1.5\%$ of the comet mass. This value is in agreement with the analytical solution proposed by Moses et al. (1999). Moses et al.’s (1999) analytical approach also estimates that a 45° oblique impact can be expected to retain ~ 3.4 times more water than a 90° impact, or about 5.1% of the cometary mass. Most of the differences between the present initial retention rate value of 3.1% and their 5.1% estimate is probably due to the simplifying assumptions used in Moses et al.’s (1999) analytic solution. Their model assumes the hemispherical expansion of an ideal gas mixture made of equal parts comet and target material by mass. However, the dynamics of an oblique impact event differ greatly from their assumption given that the water plume is non-hemispherical and water and rock are fairly well separated (Fig. 3). These factors are not easily included in an

analytic solution, suggesting some inaccuracy in their estimates for non-vertical impacts.

As the non-escaping water vapor falls back to the lunar surface, the water molecules begin to migrate based on the local surface temperature at the landing site. To observe the initial fallback pattern, an independent simulation was set-up where the lunar surface temperature is artificially fixed everywhere at 120 K and the Moon does not rotate. At this low temperature, the water molecules all stick to the surface and the initial fallback pattern can be observed without the dayside to nightside migration of water molecules that would occur with a realistic surface temperature distribution. Fig. 8 shows the mass of water deposited on the surface per square kilometer 7 days after impact, when 99.6% of the water molecules that do not escape have fallen back to the lunar surface (the remaining 0.4% are still present in the atmosphere at high altitudes and will require additional time to fall back to the surface or will remain in orbit around the Moon).

In the DSMC simulations of the water vapor plume expansion, most of the water vapor with radial velocities smaller than the escape velocity at the surface of the Moon appears to be evenly distributed around the point of impact (Fig. 7b). However, the water vapor is denser downrange than uprange of the impact (Fig. 6), resulting in the deposits observed in Fig. 8 where most of the water vapor plume remaining on the Moon after impact lands in the downrange direction with some material deposited in the cross-range direction and relatively little water landing directly upstream of the point of impact. The thickest deposits (~ 2000 kg/km²) form a ~ 200 km wide arc ~ 200 km downrange of the point of impact. Overall, the thickest parts of the primary deposit resemble an arrowhead pointing in the same direction as the pre-impact comet velocity vector. The extent of the primary deposition pattern is very broad with dense deposits (orange contours) being observed ~ 4000 km downrange and ~ 1000 km crossrange of the point of impact. Closer to the point of impact, the deposits are not as thick which can be attributed to the fact that the water vapor remaining within the hemispherical interface 21 s after impact is not simulated in the present computations. Twenty seconds after impact, the water vapor crossing the interface had radial velocities of ~ 1 km/s (Fig. 4f) and an average thermal speed of ~ 600 m/s. These molecules could land up to 600 km from the point of impact

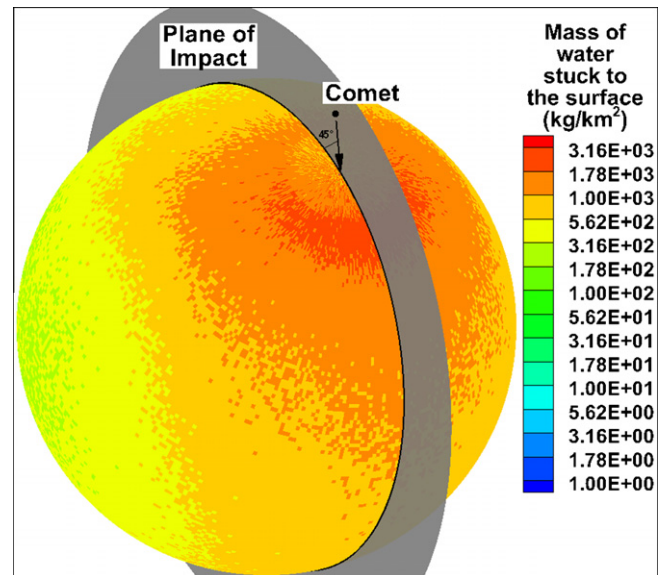


Fig. 8. Initial fallback pattern on an artificial uniformly cold lunar surface ($T_{\text{surf}} = 120$ K) for the water vapor plume after 99.6% of the molecules have fallen back to the surface. Note that the Moon does not rotate in this simulation.

assuming a ballistic trajectory and a 45° angle for the initial velocity vector (molecules with velocities of ~ 0.5 km/s could land at most 150 km from the impact crater). Uprange of the point of impact, the dense water deposits are only observed up to ~ 400 km from the point of impact. Interestingly, water molecules have landed everywhere on the lunar surface though in small quantities in regions far away from the point of impact.

3.6. Deposition in the polar cold traps

For the longer term simulations of the transient flow around the Moon, both the water in the expansion plume and the water remaining inside the crater 21 s after impact have to be modeled. In order to distinguish between the two origins of the trapped water, two independent sets of simulations were run: one only

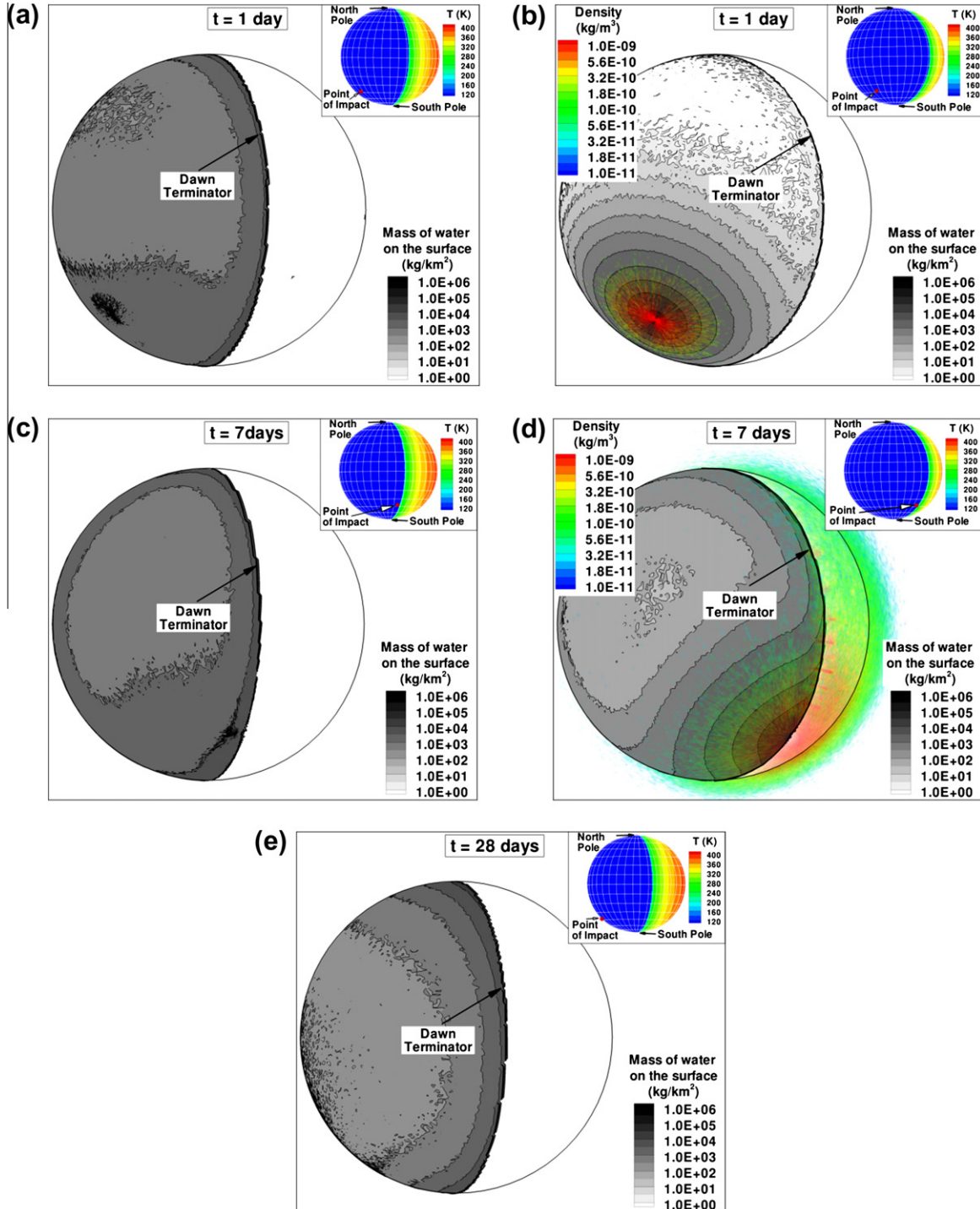


Fig. 9. Grayscale contours for the mass of water deposited on the surface per square kilometer (a) 1 day, (c) 7 days and (e) 28 days after impact for the water vapor plume simulations. Translucent density contours (colored) for the atmospheric flow with superimposed grayscale contours for the mass of water deposited on the surface per square kilometer (b) 1 day and (d) 7 days after impact for the impact crater water simulations. Note that the observer point of view is different in each figure so the inset picture indicates the location of the impact point relative to the subsolar point.

considering the vapor plume water and the other only considering the water remaining inside the crater. This assumption may influence the time at which the transient atmosphere becomes collisionless but should not greatly impact the capture rate of water in the cold traps.

For the transient flow simulations of the water in the expansion plume, the point of impact is fixed at 45° latitude at local midnight. The comet comes in at 45° from the lunar surface heading toward the South Pole. That orientation is thought to provide favorable trapping rates as some of the thick primary deposits directly land inside the South Pole cold traps (Fig. 8). The deposition patterns for the water molecules that crossed the hemispherical interface are shown 1, 7, and 28 days after impact in Fig. 9a, c and e respectively. One day after impact (Fig. 9a), most of the water on the lunar surface is deposited on the nightside south of the equator or near the terminator (thickest deposits have ~ 4000 kg/km²). No deposits are observed on the dayside because even at a relatively low dayside surface temperature of 200 K, molecules remain on the lunar surface for less than 0.02 s on average with the current residence time model. Because the timestep at this time is much greater than 0.02 s and the sampling for each snapshot is done after all the molecules have been moved, no molecule is present at all on the dayside lunar surface. Seven days after impact (Fig. 9c), the point of impact is now located at the dawn terminator. At that time, the water deposits are still asymmetric North–South but 28 days after impact (Fig. 9e), the surface contours are nearly symmetric across the equator. At that time, most of the water deposits are located near the poles and near the dawn terminator (thickest deposits have $\sim 10,000$ kg/km²) with very small water deposits present near the dusk terminator (not shown). Also note that the point of impact has almost returned to its initial position relative to the subsolar point but its actual location is barely discernable in the contours. Therefore, 1 month after impact, the transient atmospheric lunar flow has been fully established on the Moon. Initial fallout deposit patterns have been erased by dayside sublimation. From then on, the gas flow is only sustained by the sublimation of the water deposits located near the dawn terminator as the Sun rises above their location.

Only the water that did cross the SOVA interface in under 21 s was modeled in the DSMC plume simulation. The water that did not cross the SOVA interface was then modeled independently. Because the thermal properties and spatial distribution of that residual water within the crater are unknown, a fairly simple model was used to study the migration of that water to the polar cold traps: the water simply sublimates from a 30 km radius “crater” at an exponentially decaying rate over a period of time. This is intended to model the ill constrained effects of gradual cooling of the crater and percolation of water out through the pulverized overburden. Relatively fast (under 10 min) and slow releases (~ 1 month), however, provided similar results suggesting that this arbitrary release rate does not impact the final amount of water retained. The atmospheric water vapor densities and the mass of water stuck to the surface per square kilometer are presented in Fig. 9(b) 1 day and (d) 7 days) after the beginning of the release. One day after the sublimation began (Fig. 9b), only a small fraction of the sublimated water has reached the sunlit part of the lunar atmosphere. Water molecules are deposited into concentric circles on the nightside of the Moon with the densest deposits ($\sim 6 \times 10^5$ kg/km²) occurring near the impact crater. At that time, some of the water has been deposited near the South Pole region and some thin deposits can also be observed near the terminator. Seven days after the beginning of the release (Fig. 9d), the impact point is located near the dawn terminator. At this time, the fullest atmosphere is mostly localized near the impact crater and the southern dawn terminator. A small fraction of the water molecules have, however, travelled to the northern hemisphere and slightly thicker deposits

are observed near the terminator north of the equator. The densest deposits are still observed near the point of impact 7 days after impact.

Line plots for the total mass of water captured in the polar cold traps are shown in Fig. 10. In this figure, both the water that crossed the SOVA interface and the water that remained within the interface are being considered. Capture of the cometary water starts early on during the migration process (inset in Fig. 10). Ten hours after impact almost $\sim 1 \times 10^8$ kg of water was captured in the South Pole cold traps near the point of impact, much of this is simply from the initial ballistic fallout. In comparison, only $\sim 1.75 \times 10^7$ kg was captured in the North Pole cold trap by that time. The photodestruction (“Mass Lost” in Fig. 10) of the water is, however, noticeably faster than the capture rate as $\sim 9 \times 10^9$ kg has already been destroyed after ten hours. The atmosphere is assumed to be thin so that the incident photons can hit any molecule present in the dayside atmosphere. This assumption means that, at least initially, more molecules are destroyed than should be because some of the lower layers of the dayside atmosphere should be partially shielded from photo-reaction processes.

As the Moon rotates, water molecules continue to accumulate into both southern and northern poles at similar rates. The small oscillations that are more noticeable in the “mass lost” line (square symbols) are due to a fluctuating number of molecules in the lunar atmosphere due to the Sun rising over relatively larger/smaller deposits. Six months after impact, $\sim 4.6 \times 10^9$ kg of water is trapped at the South Pole, $\sim 1.8 \times 10^9$ kg is trapped at the North Pole and $\sim 1.3 \times 10^{11}$ kg has been lost. These quantities account for 74% of the water remaining on the Moon at that time. Assuming that the rates for all quantities from 6 months on remain constant, $\sim 0.14\%$ of the comet initial mass is trapped in the lunar cold traps for an impact point located at latitude 45° with the impact event occurring at local midnight. This fraction of the comet mass yields 6.51×10^9 kg of water captured in the polar cold traps. With a trapping surface area of 5832 km², the deposits are equivalent to 1.12 kg/m² or an ice layer thickness of ~ 1 mm. Two other impact locations and impact times were also tested in the transient flow simulations of the water initially remaining inside the impact crater: impact at the 45° latitude at local noon and impact at the North Pole. Overall trapping rates for all three cases were very similar, with slightly higher retention observed for the North Pole

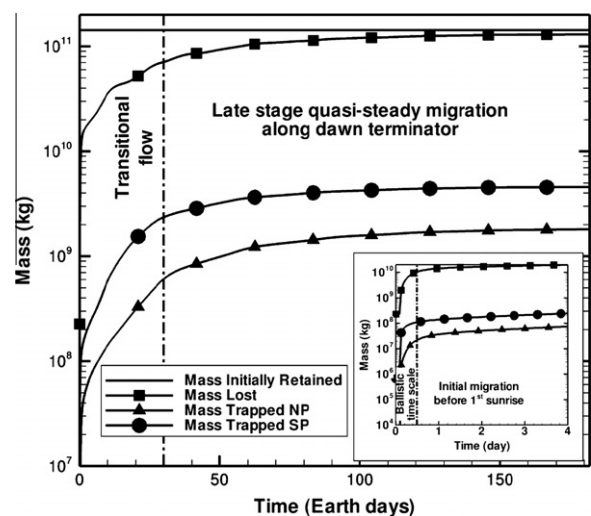


Fig. 10. Mass of water initially retained (no symbol), that is destroyed (square symbol), and is captured in the cold traps (circle and triangle symbols for the cold traps located at the South Pole and North Pole, respectively) as a function of time. The inset figure zooms into early times. Note that the lines start three hours after impact when the intermediate simulations were started.

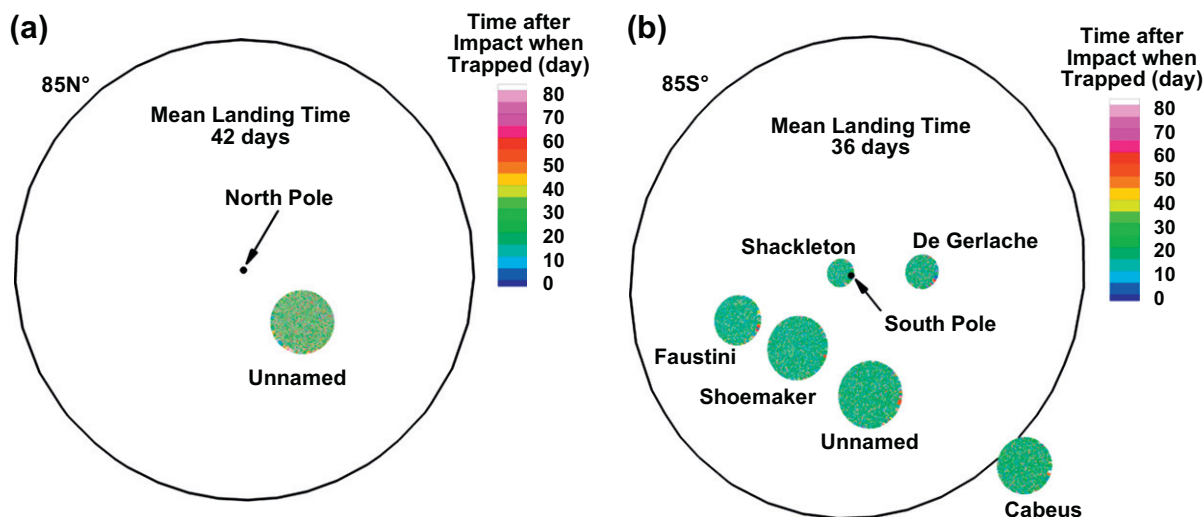


Fig. 11. Scatter plot of the deposition pattern of water ice in the North Pole cold trap (left) and in the South Pole cold traps (right). The color scale represents the time at which the molecules are trapped.

impact point location as more water landed directly into a cold trap. However, in that case the distribution of trapped water is noticeably different, with more water being captured at the North Pole than at the South Pole, opposite to what is observed in the other two cases.

The deposition pattern of water inside the modeled cold traps is shown 6 months after impact in Fig. 11 for the impact point located at the 45°S latitude. The typical radius of a polar cold trap is much smaller than the distance travelled by a molecule during a ballistic hop at the mean temperature observed on the lunar surface. Therefore, the location at which a molecule lands in a polar cold trap is random and a near uniform distribution is observed in the cold traps. Fig. 11 also shows that, on average, molecules landed in the South Pole cold traps earlier (bluer¹ colors) than in the North Pole cold trap (greener colors). The difference between the mean trapping times is due to the chosen location for the point of impact near the South Pole.

3.7. Final retention rate estimates

Ong et al. (2010) estimated that the total water mass flux to the Moon due to comet impacts over 1 byr was between 1.9×10^5 to 6.0×10^6 kg/year. They then estimated the fraction of water retained on the Moon by normalizing their modeled fraction of water retained as function of velocity by the probability that an impact occurs at a given velocity. Note that the mass retained refers to the mass left on the Moon after impact and not the mass captured inside the cold traps. They considered comet sizes from 500 m to 34 km in diameter by extending their modeled fraction of water retained as function of velocity for the impact of a 2 km diameter ice sphere (the comet) to the entire range of comet sizes. Using the same approach and using Ong et al.'s (2010) cometary flux and size distributions, we estimate that about 9.6% of the water mass delivered to the Moon by comet impacts is retained on the Moon, before accounting for loss mechanisms during migration and gardening in the polar cold traps, which amounts to 1.8×10^{13} – 5.8×10^{14} kg of water over 1 byr. We also found that about 5% of the water molecules retained on the Moon after impact are actually captured in the cold traps or 9.0×10^{11} – 2.9×10^{12} kg over 1 byr. The fraction of water destroyed inside the cold traps

was estimated to be 94.4% (Crider and Vondrak, 2003), so as a low estimate, about 5.0×10^{10} – 1.6×10^{11} kg of water should be present inside the polar cold traps after 1 byr. These values are on the low end of Ong et al.'s (2010) estimates for the mass of water being present at the lunar poles (1.3×10^{11} – 4.3×10^{12} kg). From the Lunar Prospector data, Feldman et al. (2000) estimated that as much as 1.98×10^{11} kg of water ice may be present at the lunar poles. Using a method similar to that of Feldman et al. (2000) to estimate how much water may be present at the polar cold traps and assuming that Cabeus is representative of the lunar polar cold traps; Colaprete et al. (2010) estimates of a concentration of water by mass at the impact site of $5.6 \pm 2.9\%$ translate into as much as 7.4×10^{11} kg of water ice being present at the lunar poles. The present values are therefore at the low end of previous estimates and of both the Lunar Prospector and LCROSS observations.

4. Conclusions

The primary purpose of this study was to model the water vapor flow produced by a comet impact on the Moon using a hybrid SOVA–DSMC approach. The initial conditions for the modeled comet impact were chosen to be fairly representative of the most probable impact event: a 45° oblique impact of a 1 km radius ice sphere at 30 km/s. The SOVA hydrocode simulated the physics of the impact event up to a few tens of kilometers from the point of impact and the DSMC solver simulated the evolution of the water vapor from the SOVA/DMSC hemispherical interface until it was either lost due to escape, destroyed by photodestruction processes, or captured inside one of the lunar polar cold traps months after impact.

Initially, most of the water vapor moves radially out through the downrange portion of the interface with velocities up to 50 km/s. Because of the very high velocities early on, most of the water crossing the 20 km radius hemispherical interface in under seven seconds is lost due to planetary escape. The shape of the plume is initially very complex but the downrange part of the plume becomes quickly surrounded (in less than 5 s) by the ejecta curtain that takes on the shape of an inverted cone consistent with observations in impact experiments. As more water vapor crosses the interface a secondary low density plume can be observed uprange of the main high density plume. Simultaneously, a

¹ For interpretation of color in Figs. 3, 8 and 11, the reader is referred to the web version of this article.

target-rich plume rises from the center of the expanding crater. This rock-dominated plume pushes water out of its way, limiting the main vapor plume to an outer ring of high density water. Overall, the extent of the plume at the interface is greater uprange of the point of impact but because most of the uprange material has low density, most of the water vapor is moving downrange of the point of impact. Starting ten seconds after impact, most of the water vapor crosses the hemispherical interface with velocities slower than the escape velocity. The flow is highly supersonic so the plume mostly expands radially with time and very little broadening of the plume due to thermal motion can be observed up to a few tens of seconds after impact. The plume is also relatively cold, with the hottest gas being the water vapor that crossed the interface shortly after impact (in less than one second) and nearly entirely continuum up to several tens of seconds after impact.

Most of the water vapor plume escapes the gravity well of the Moon within the first few hours after impact. For such a large comet impact, only ~3% of the comet mass remains on the Moon after impact. Of this total mass 2% crossed the SOVA interface under 21 s while less than 1% was still within the interface at the end of the SOVA computations. As the Moon rotates, initially retained water molecules begin to migrate until they are destroyed or captured in a cold trap. Since recombination processes for the photo-dissociation products and possible shielding of molecules in the lower layers of the vapor cloud from solar photons were ignored in the model, the results represent a lower limit estimate of mass captured in the cold traps. Of the original comet's mass remaining on the Moon after impact, only a small fraction, about 0.14%, actually reaches the cold traps. Based on the surface area of the cold traps used in the simulation, ~1 mm of ice will have accumulated in the polar cold traps after impact. Using the results presented by Ong et al. (2010) and Crider and Vondrak (2003), between 5.0×10^{10} and 1.6×10^{11} kg of water should have accumulated inside the polar cold traps after 1 byr, consistent with previous estimates (Ong et al., 2010). From the Lunar Prospector data, Feldman et al. (2000) estimated that as much as 1.98×10^{11} kg of water ice may be present at the lunar poles. From the Chandrayaan mission, it was estimated that at least 6×10^{11} kg of water ice was present in the lunar cold traps (at http://www.nasa.gov/mission_pages/Mini-RF/multimedia/feature_ice_like_deposits.html). From the LCROSS data, it was estimated that as much as 7.4×10^{11} kg of water ice may be present at the lunar poles. Therefore, the present estimates are consistent with the Lunar Prospector, the Chandrayaan and the LCROSS observations.

Acknowledgments

The authors thank Erik Asphaug and an anonymous reviewer for their useful comments that improved this manuscript. This work is sponsored by the NASA Planetary Atmospheres and LASER programs. The authors also would like to acknowledge the Texas Advanced Computing Center (TACC) at The University of Texas at Austin for providing substantial computing resources.

References

Anderson, C.E., 1987. An overview of the theory of hydrocodes. *Int. J. Impact Eng.* 5, 33–59.
 Arnold, J.R., 1979. Ice in the lunar polar regions. *J. Geophys. Res.* 84, 5659–5668.
 Artemieva, N.A., Shuvalov, V.V., 2008. Numerical simulation of high-velocity impact ejecta following falls of comets and asteroids onto the Moon. *Solar Syst. Res.* 42, 329–334.
 Berezhnoi, A.A., Klumov, B.A., 1998. Lunar ice: Can its origin be determined? *JETP Lett.* 68, 163–167.
 Bird, G.A., 1994. *Molecular Gas Dynamics and the Direct Simulation of Gas Flow*. Oxford University Press, New York.
 Butler, B.J., 1997. The migration of volatiles on the surfaces of Mercury and the Moon. *J. Geophys. Res.* 102, 19283–19291.

Campbell, B.A., Campbell, D.B., 2006. Regolith properties in the south polar region of the Moon from 70-cm radar polarimetry. *Icarus* 180, 1–7.
 Campbell, B.A., Campbell, D.B., Chandler, J.F., Hine, A.A., Nolan, M.C., Perillat, P.J., 2003. Radar imaging of the lunar poles. *Nature* 426, 137–138.
 Clark, R.N., 2009. Detection of Adsorbed Water and Hydroxyl on the Moon. *Science Express Reports*. doi:10.1126/science.1178105.
 Colaprete, A. et al., 2010. Detection of water in the LCROSS Ejecta Plume. *Science* 330, 463–468.
 Crider, D.H., Vondrak, R.R., 2000. The solar wind as a possible source of lunar polar hydrogen deposits. *J. Geophys. Res.* 105, 26773–26782.
 Crider, D.H., Vondrak, R.R., 2002. Hydrogen migration to the lunar poles by solar wind bombardment of the Moon. *Adv. Space Res.* 30, 1869–1874.
 Crider, D.H., Vondrak, R.R., 2003. Space weathering effects on lunar cold trap deposits. *J. Geophys. Res.* 108, 5079. doi:10.1029/2002JE002030.
 Dietrich, S., Boyd, I.D., 1996. Scalar and parallel optimized implementation of the Direct Simulation Monte Carlo method. *J. Comput. Phys.* 126, 328–342.
 Eke, V.R., Teodoro, L.F.A., Elphic, R.C., 2009. The spatial distribution of polar hydrogen deposits on the Moon. *Icarus* 200, 12–18.
 Elphic, R.C., Eke, V.R., Teodoro, L.F.A., Lawrence, D.J., Bussey, D.B.J., 2007. Models of the distribution of hydrogen at the lunar south pole. *Geophys. Res. Lett.* 34, L13204. doi:10.1029/2007GL029954.
 Feldman, W.C. et al., 1998. Major compositional units of the Moon: Lunar Prospector thermal and fast neutrons. *Science* 281, 1489–1493.
 Feldman, W.C., Lawrence, D.J., Elphic, R.C., Barraclough, B.L., Maurice, S., Genetay, I., Binder, A.B., 2000. Polar hydrogen deposits on the Moon. *J. Geophys. Res.* 105, 4175–4195.
 Frenkel, Z., 1924. Theorie der adsorption und verwandter erscheinungen. *Z. Phys.* 26, 117–138.
 Garcia, A.L., Wagner, W., 2006. Generation of the Maxwellian inflow distribution. *J. Comput. Phys.* 217, 693–708.
 Goldstein, D.B., Stern, S.A., Crider, D.H., Gladstone, G.R., Durda, D.D., Asphaug, E., Larignon, B., Varghese, P.L., Trafton, L.M., 2007. Free molecular simulations of vapor dynamics following a lunar impact. In: *Rarefied Gas Dynamics: 25th International Symposium*, Published by the Siberian Branch of the Russian Academy of Sciences.
 Hodges, R.R., 1991. Exospheric transport restrictions on water ice in lunar polar traps. *Geophys. Res. Lett.* 18, 2113–2116.
 Hodges, R.R., 2002. Reanalysis of Lunar Prospector neutron spectrometer observations over the lunar poles. *J. Geophys. Res.* 107, 5125. doi:10.1029/2000JE001483.
 Huebner, W.F., Keady, J.J., Lyon, S.P., 1992. Solar photo rates for planetary atmospheres and atmospheric pollutants. *Astrophys. Space Sci.* 195, 1–294.
 Langmuir, I., 1916. The evaporation, condensation and reflection of molecules and the mechanism of adsorption. *Phys. Rev.* 8, 149–176.
 Lawrence, D.J., Feldman, W.C., Elphic, R.C., Hagerty, J.J., Maurice, S., McKinney, G.W., Prettyman, T.H., 2006. Improved modeling of Lunar Prospector neutron spectrometer data: Implications for hydrogen deposits at the lunar poles. *J. Geophys. Res.* 111, E08001. doi:10.1029/2005JE002637.
 LeBeau, G.J., 1999. A parallel implementation of the Direct Simulation Monte Carlo method. *Comput. Method Appl. Mech. Eng.* 174, 319–337.
 Li, Z., Zhong, J., Levin, D.A., Garrison, B.J., 2009. Kinetic nucleation model for free expanding water condensation plume simulations. *J. Chem. Phys.* 130, 174309. doi:10.1063/1.3129804.
 Lilley, C.R., Macrossan, M.N., 2003. Methods for implementing the stream boundary condition in DSMC computations. *Int. J. Numer. Method. Fluids* 42, 1363–1371.
 Macrossan, M.N., Geng, X., 2007. Detecting equilibrium cells in DSMC to improve the computational efficiency. In: *Rarefied Gas Dynamics: 25th International Symposium*, Published by the Siberian Branch of the Russian Academy of Sciences, pp. 361–366.
 Margot, J.L., Campbell, D.B., Jurgens, R.F., Slade, M.A., 1999. Topography of the lunar poles from radar interferometry: A survey of cold trap locations. *Science* 284, 1658–1660.
 Melosh, H.J., 1989. *Impact Cratering – A Geologic Process*. Oxford University Press, New York, pp. 46–86.
 Melosh, H.J., 2007. A hydrocode equation of state for SiO₂. *Meteorit. Planet. Sci.* 42, 2079–2098.
 Morgan, T.H., Shemansky, D.E., 1991. Limits to the lunar atmosphere. *J. Geophys. Res.* 96, 1351–1367.
 Moses, J.I., Rawlins, K., Zahnle, K., Dones, L., 1999. External sources of water for Mercury putative ice deposits. *Icarus* 137, 197–221.
 Nanbu, K., 1986. Theoretical basis of the Direct Simulation Monte Carlo method. In: *Rarefied Gas Dynamics: 15th International Symposium Proceedings 1*, Teubner, Stuttgart, pp. 369–383.
 Noda, H., Araki, H., Goossens, S., Ishihara, Y., Matsumoto, K., Tazawa, S., Kawano, N., Sasaki, S., 2008. Illumination conditions at the lunar polar regions by KAGUYA (SELENE) laser altimeter. *Geophys. Res. Lett.* 35, L24203. doi:10.1029/2008GL035692.
 Nozette, S., Lichtenberg, C.L., Spudis, P., Bonner, R., Ort, W., Malaret, E., Robinson, M., Shoemaker, E.M., 1996. The Clementine bistatic radar experiment. *Science* 274, 1495–1498.
 Ong, L., Asphaug, E.L., Korycansky, D., Coker, R.F., 2010. Volatile retention from cometary impacts on the Moon. *Icarus* 207, 578–589.
 Pierazzo, E., Melosh, H.J., 2000a. Understanding oblique impacts from experiments, observations, and modeling. *Annu. Rev. Earth Planet. Sci.* 28, 141–167.
 Pierazzo, E., Melosh, H.J., 2000b. Hydrocode modeling of oblique impacts: The fate of the projectile. *Meteorit. Planet. Sci.* 35, 117–130.

- Pierazzo, E., Vickery, A.M., Melosh, H.J., 1997. A reevaluation of impact melt production. *Icarus* 127, 408–423.
- Pierazzo, E. et al., 2008. Validation of numerical codes for impact and explosion cratering. *Meteorit. Planet. Sci.* 43, 1917–1938.
- Pieters, C.M. et al., 2009. Character and Spatial Distribution of OH/H₂O on the Surface of the Moon Seen by M³ on Chandrayaan-1. *Science Express Reports*. doi:10.1126/science.1178658.
- Roveda, R., Goldstein, D.B., Varghese, P.L., 2000. Hybrid Euler/Direct Simulation Monte Carlo calculation of unsteady slit flow. *J. Spacecraft Rockets* 37, 753–760.
- Sandford, S.A., Allamandola, L.J., 1988. The condensation and vaporization behavior of H₂O:CO ices and implications for interstellar grains and cometary activity. *Icarus* 76, 201–224.
- Schultz, P., Hermalyn, B., Colaprete, A., Ennico, K., Shirley, M., Marshall, W., 2010. The LCROSS cratering experiment. *Science* 330, 468–472.
- Shuvalov, V.V., 1999. Multi-dimensional hydrodynamic code SOVA for interfacial flows: Application to the thermal layer effect. *Shock Waves* 9, 381–390.
- Simpson, R.A., Tyler, G.L., 1999. Reanalysis of Clementine bistatic radar data from the lunar south pole. *J. Geophys. Res.* 104, 3845–3862.
- Stacy, N.J.S., Campbell, D.B., Ford, P.G., 1997. Arecibo radar mapping of the lunar poles: A search for ice deposits. *Science* 276, 1527–1530.
- Starukhina, L.V., Shkuratov, Y.G., 2000. The lunar poles: Water ice or chemically trapped hydrogen? *Icarus* 147, 585–587.
- Stern, S.A., 1999. Lunar atmosphere: History, status current problems and context. *Rev. Geophys.* 37, 453–491.
- Stewart, B., Pierazzo, E., Goldstein, D., Varghese, P., Trafton, L., Moore, C., 2009. Parallel 3D Hybrid Continuum/DSMC Method for Unsteady Expansions into a Vacuum. 47th AIAA Aerospace Sciences Meeting, Orlando, Florida, AIAA 2009-266.
- Sunshine, J.M., Farnham, T.L., Feaga, L.M., Groussin, O., Merlin, F., Milliken, R.E., A'Hearn, M.F., 2009. Temporal and Spatial Variability of Lunar Hydration as Observed by the Deep Impact Spacecraft. *Science Express Reports*. doi:10.1126/science.1179788.
- Thompson, S.L., Lauson, H.S., 1972. Improvements in the Chart-D Radiation Hydrodynamic Code III: Revised Analytical Equation of State. Tech. Rep. SC-RR-710714 (Sandia Nat. Labs.).
- Titov, E.V., Levin, D.A., 2007. Extension of the DSMC method to high pressure flows. *Int. J. Comput. Fluid Dyn.* 21, 351–368.
- Turtle, E.P., Pierazzo, E., 2001. Thickness of a European ice shell from impact crater simulations. *Science* 294, 1326–1328.
- Vasavada, A.R., Paige, D.A., Wood, S.E., 1999. Near-surface temperatures on Mercury and the Moon and the stability of polar ice deposits. *Icarus* 141, 179–193.
- Walker, A.C., Gratiy, S.L., Goldstein, D.B., Moore, C.H., Varghese, P.L., Trafton, L.M., Levin, D.A., Stewart, B., 2010. A comprehensive numerical simulation of Io's sublimation-driven atmosphere. *Icarus* 207, 394–408.
- Watson, K., Murray, B.C., Brown, H., 1961. The behavior of volatiles on the lunar surface. *J. Geophys. Res.* 66, 3033–3045.
- Wu, J.-S., Tseng, K.-C., 2005. Parallel DSMC method using dynamic domain decomposition. *Int. J. Numer. Method. Eng.* 63, 37–76.
- Zhang, J., Goldstein, D.B., Varghese, P.L., Gimelshein, N.E., Gimelshein, S.F., Levin, D.A., 2003. Simulation of gas dynamics and radiation in volcanic plumes on Io. *Icarus* 163, 182–197.
- Zhang, J., Goldstein, D.B., Varghese, P.L., Trafton, L.M., Miki, K., Moore, C., 2004. Numerical modeling of Ionian volcanic plumes with entrained particulates. *Icarus* 172, 479–502.
- Zhong, J., Zeifman, M.I., Levin, D.A., Gimelshein, S.F., 2005. Direct Simulation Monte Carlo modeling of homogeneous condensation in supersonic plumes. *AIAA J.* 43, 1784–1796.